

# Bifunctional hydroformylation on heterogeneous Rh-WO<sub>x</sub> pair site catalysts

<https://doi.org/10.1038/s41586-022-05075-4>

Received: 4 November 2021

Accepted: 5 July 2022

Published online: 7 September 2022

 Check for updates

Insoo Ro<sup>1,2,3,10</sup>, Ji Qi<sup>1,3,10</sup>, Seungyeon Lee<sup>3,4,10</sup>, Mingjie Xu<sup>5</sup>, Xingxu Yan<sup>5</sup>, Zhenhua Xie<sup>6,7</sup>, Gregory Zakem<sup>1</sup>, Austin Morales<sup>1</sup>, Jingguang G. Chen<sup>6,7</sup>, Xiaoqing Pan<sup>5,8,9</sup>, Dionisios G. Vlachos<sup>3,4</sup>, Stavros Caratzoulas<sup>4</sup> & Phillip Christopher<sup>1,3</sup>✉

Metal-catalysed reactions are often hypothesized to proceed on bifunctional active sites, whereby colocalized reactive species facilitate distinct elementary steps in a catalytic cycle<sup>1–8</sup>. Bifunctional active sites have been established on homogeneous binuclear organometallic catalysts<sup>9–11</sup>. Empirical evidence exists for bifunctional active sites on supported metal catalysts, for example, at metal–oxide support interfaces<sup>2,6,7,12</sup>. However, elucidating bifunctional reaction mechanisms on supported metal catalysts is challenging due to the distribution of potential active-site structures, their dynamic reconstruction and required non-mean-field kinetic descriptions<sup>7,12,13</sup>. We overcome these limitations by synthesizing supported, atomically dispersed rhodium–tungsten oxide (Rh-WO<sub>x</sub>) pair site catalysts. The relative simplicity of the pair site structure and sufficient description by mean-field modelling enable correlation of the experimental kinetics with first principles-based microkinetic simulations. The Rh-WO<sub>x</sub> pair sites catalyse ethylene hydroformylation through a bifunctional mechanism involving Rh-assisted WO<sub>x</sub> reduction, transfer of ethylene from WO<sub>x</sub> to Rh and H<sub>2</sub> dissociation at the Rh-WO<sub>x</sub> interface. The pair sites exhibited >95% selectivity at a product formation rate of 0.1 g<sub>propanal</sub> cm<sup>−3</sup> h<sup>−1</sup> in gas-phase ethylene hydroformylation. Our results demonstrate that oxide-supported pair sites can enable bifunctional reaction mechanisms with high activity and selectivity for reactions that are performed in industry using homogeneous catalysts.

Here we examine bifunctional active sites at heterogeneous Rh-WO<sub>x</sub> interfaces with structures ranging from atomically dispersed to three-dimensional domains, as each species exhibits structure-dependent reactivity<sup>14,15</sup>. We focus on alkene hydroformylation, in which an alkene, CO and H<sub>2</sub> react to add a formyl (CHO) group and H across the C=C double bond to produce an aldehyde<sup>16</sup>. Alkene hydroformylation proceeds industrially on homogeneous Rh catalysts with close to quantitative selectivity for aldehyde formation<sup>17</sup>. Oxide-supported Rh catalysts show undesired alkene hydrogenation and secondary product formation in gas-phase flow reactors (Supplementary Table 1) and are saturated by adsorbed CO during hydroformylation, thus limiting their reaction rates. Alternatively, WO<sub>x</sub> strongly interacts with alkenes during metathesis, which occurs at similar temperatures to hydroformylation<sup>18</sup>. This led to the hypothesis that colocalized Rh and WO<sub>x</sub> species could interact with distinct reactants during alkene hydroformylation and overcome the limitations of Rh catalysts.

## Controlling Rh and WO<sub>x</sub> structure

Catalysts were synthesized by first depositing WO<sub>x</sub> onto γ-Al<sub>2</sub>O<sub>3</sub> (144 m<sup>2</sup> g<sup>−1</sup>), followed by Rh. The WO<sub>x</sub> structure was controlled by

varying the weight loading. Spectroscopic characterization demonstrated that WO<sub>x</sub> existed as isolated species at 0.7 wt% W, as isolated and two-dimensional (2D) oligomers at 2 wt% and as three-dimensional (3D) structures at >8 wt% (Fig. 1a, Supplementary Fig. 1 and Supplementary Table 2)<sup>19,20</sup>. W was in the +6 oxidation state following calcination (Supplementary Fig. 1 and Supplementary Table 2). Rh was deposited via strong electrostatic adsorption of a cationic Rh<sup>3+</sup> precursor, followed by calcination at 623 K (Supplementary Fig. 2 and Supplementary Table 3), which maintained Rh<sup>3+</sup> (Supplementary Fig. 3). The Rh weight loading was constant in all catalysts (0.23–0.29%). The catalysts are denoted as Rh/xW, where x is the loading of W.

Figure 1b and Supplementary Fig. 4 show high-angle annular dark-field scanning transmission electron microscopy (HAADF-STEM) images of Rh/0.7W. The different intensities in the HAADF-STEM image for each atom in identified atomically dispersed pairs demonstrate the formation of Rh-W pair sites on the basis of element-specific electron scattering cross-sections (scattering ∝ (atomic number, Z)<sup>1.5–2</sup>) of Rh (Z = 45) and W (Z = 74) (Fig. 1c)<sup>21</sup>. HAADF-STEM images of Rh/2W (Supplementary Fig. 5) show sub-nm clusters and atomically dispersed species, which is consistent with the spectroscopy (Supplementary Fig. 1). Imaging and elemental mapping of Rh/24.5W (Fig. 1d,e and Supplementary Fig. 6)

<sup>1</sup>Department of Chemical Engineering, University of California, Santa Barbara, Santa Barbara, CA, USA. <sup>2</sup>Department of Chemical and Biomolecular Engineering, Seoul National University of Science and Technology, Seoul, Republic of Korea. <sup>3</sup>Catalysis Center for Energy Innovation, Newark, DE, USA. <sup>4</sup>Department of Chemical and Biomolecular Engineering, University of Delaware, Newark, DE, USA. <sup>5</sup>Department of Materials Science and Engineering, University of California Irvine, Irvine, CA, USA. <sup>6</sup>Chemistry Division, Brookhaven National Laboratory, Upton, NY, USA. <sup>7</sup>Department of Chemical Engineering, Columbia University, New York, NY, USA. <sup>8</sup>Department of Physics and Astronomy, University of California, Irvine, Irvine, CA, USA. <sup>9</sup>Irvine Materials Research Institute (IMRI), University of California Irvine, Irvine, CA, USA. <sup>10</sup>These authors contributed equally: Insoo Ro, Ji Qi, Seungyeon Lee. ✉e-mail: pchristopher@ucsb.edu

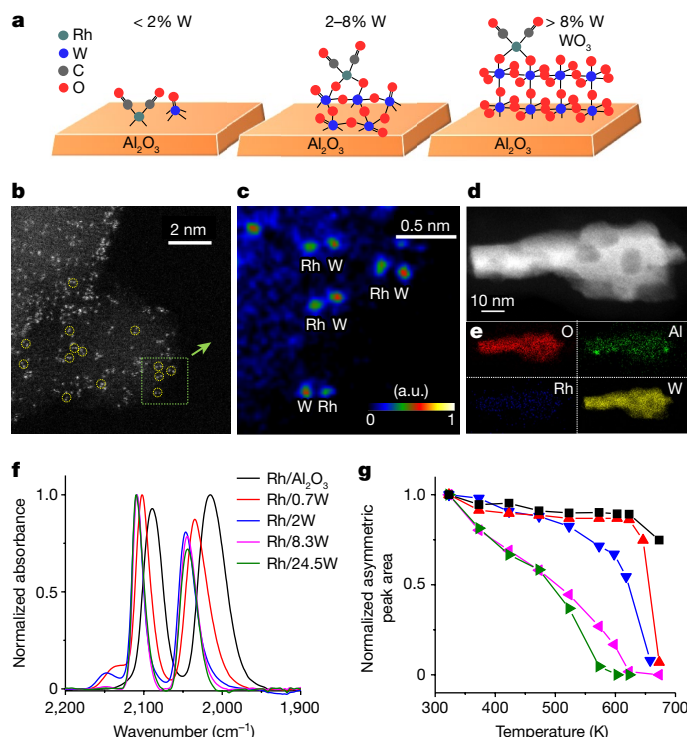


**Fig. 1 | Coordination of atomically dispersed Rh to WO<sub>x</sub> with varying structure.** **a**, Schematic illustration of Rh/*x*W structures as a function of W loading. The elements are colour coded as follows: red, O; green, Rh; blue, W; grey, C. **b**, Representative STEM image of Rh/0.7W. Atomically dispersed pairs are circled in yellow. **c**, False-coloured STEM image of the area outlined in **b**. False coloration is based on the scattering intensity. **d**, **e**, STEM image (**d**) and EDS map (**e**) of Rh/24.5W. Images were collected after ex situ CO pretreatment at 523 K. **f**, CO probe molecule FTIR spectra collected at saturation CO coverage under Ar flow at 298 K, after in situ pretreatment at 523 K in CO. Spectra are normalized to the maximum intensity of the CO stretch. **g**, Relative intensity of the CO asymmetric stretch as a function of temperature from 323 to 673 K during TPD executed at a linear ramp rate of 20 K min<sup>-1</sup> in 100 sccm of Ar flow.

indicate that Al<sub>2</sub>O<sub>3</sub> was covered by W, consistent with the spectroscopic analyses that suggested bulk WO<sub>3</sub> was formed. Whereas Rh was present in elemental maps, the strong electron scattering by W made it difficult to characterize the Rh structure in Rh/24.5W.

Figure 1f shows CO probe molecule Fourier transform infrared (FTIR) spectra of the catalysts. CO stretches at 2,110–2,088 and 2,045–2,015 cm<sup>-1</sup> were assigned to the symmetric and asymmetric stretches of atomically dispersed Rh<sub>gem</sub>-dicarbonyl species (Rh(CO)<sub>2</sub>), respectively (Supplementary Fig. 7)<sup>22</sup>. The absence of stretches at approximately 2,070 and 1,860 cm<sup>-1</sup>, associated with linear and bridge-bound CO on metallic Rh clusters, demonstrates that Rh species were atomically dispersed (Supplementary Fig. 8). The symmetric stretch of Rh(CO)<sub>2</sub> shifted from 2,089 cm<sup>-1</sup> to 2,110 cm<sup>-1</sup> when comparing Rh/Al<sub>2</sub>O<sub>3</sub> and Rh/2W, and was constant at W loadings >2% (see Supplementary Table 4). Rh/0.7W exhibited a single pair of symmetric and asymmetric Rh(CO)<sub>2</sub> stretches, suggesting a majority of Rh was paired with W. The small 2,150–2,135 cm<sup>-1</sup> shoulder for Rh/0.7W and Rh/2W is assigned to Rh(CO)(O), which forms due to incomplete reduction of Rh<sup>2+</sup>.

Temperature-programmed desorption (TPD) of CO from Rh(CO)<sub>2</sub> showed that Rh/0.7W exhibited an approximate 25 K decrease in the onset temperature of CO desorption compared to Rh/Al<sub>2</sub>O<sub>3</sub>, whereas the desorption onset decreased by approximately 150 K for Rh on 2D WO<sub>x</sub> domains (Rh/2W), and by approximately 300 K for Rh on 3D WO<sub>x</sub> domains (Rh/8 and 24.5W) (Fig. 1g and Supplementary Figs. 9 and 10). On the basis of the similar shifts in CO vibrational frequency and CO desorption temperature, it is hypothesized that at W loadings of >2% Rh

sat on top of 2D and 3D WO<sub>x</sub> domains. STEM images of Rh/0.7W suggest that here Rh sat adjacent to atomically dispersed WO<sub>x</sub>.

## Catalytic reactivity for ethylene hydroformylation

Gas-phase ethylene hydroformylation primarily produces propanal (desired hydroformylation), ethane (undesired hydrogenation) and propanol (propanal hydrogenation). Steady-state differential reactivity measurements at 423 K and 1 bar in the absence of transport limitations (Supplementary Fig. 11, Supplementary Note 1 and Supplementary Tables 5 and 6) showed that Rh/0.7W exhibited the highest propanal formation turnover frequency (TOF) (18× and 5× greater than Rh/Al<sub>2</sub>O<sub>3</sub> and Rh/24.5W, respectively) and selectivity (53% versus 16% for Rh/Al<sub>2</sub>O<sub>3</sub>, and 40% for Rh/24.5W) of the Rh/*x*W/Al<sub>2</sub>O<sub>3</sub> catalysts (see Supplementary Fig. 12). Ethane and propanol were the only observed products, demonstrating that Rh remained atomically dispersed (Supplementary Fig. 13). Rh/0.7W exhibited the lowest apparent activation barrier (*E*<sub>app</sub>) for propanal formation (Fig. 2a).

Propanal TOF exhibited a positive order in CO concentration ( $\alpha_{\text{CO,propanal}}$ ) for Rh/0.7W. Catalysts not containing Rh-W pair sites exhibited negative  $\alpha_{\text{CO,propanal}}$  (Fig. 2b), consistent with previous reports of oxide-supported Rh catalysts (Supplementary Table 1)<sup>23</sup>. The negative  $\alpha_{\text{CO,propanal}}$  for atomically dispersed Rh active sites is a result of quasi-equilibrated CO adsorption that saturates Rh sites (Rh(CO)<sub>2</sub> is the most common intermediate under the reaction conditions)<sup>24</sup>, CO desorption from Rh(CO)<sub>2</sub> initiating the catalytic cycle<sup>23</sup> and the need for two adjacent sites on Rh for propanal formation (see Supplementary Fig. 14 and Supplementary Tables 1 and 7).

In situ FTIR showed Rh(CO)<sub>2</sub> as the dominant Rh species for Rh/0.7W, suggesting that neighbouring WO<sub>x</sub> mitigated the negative  $\alpha_{\text{CO}}$ , propanal as seen for other catalysts, without notably changing the steady-state coverage of CO on Rh. Previous analysis of Rh-ReO<sub>x</sub>/Al<sub>2</sub>O<sub>3</sub> pair sites found kinetic parameters consistent with Rh/Al<sub>2</sub>O<sub>3</sub> (negative  $\alpha_{\text{CO,propanal}}$ ), demonstrating the distinct behaviour of Rh-ReO<sub>x</sub> and Rh-WO<sub>x</sub> pair sites<sup>21</sup>. Rh/0.7W exhibited different dependencies for propanal TOF on C<sub>2</sub>H<sub>4</sub> concentration (Fig. 2b) and ethane TOF on CO and C<sub>2</sub>H<sub>4</sub> concentration (Supplementary Fig. 15) compared with other catalysts.

Steady-state H<sub>2</sub>/D<sub>2</sub> kinetic isotope effect (KIE, rate<sub>H<sub>2</sub></sub>/rate<sub>D<sub>2</sub></sub>) measurements for Rh/Al<sub>2</sub>O<sub>3</sub>, Rh/0.7W and Rh/24.5W showed KIEs for propanal formation of 1.04 ± 0.02, 2.02 ± 0.01 and 1.03 ± 0.04, respectively (Supplementary Fig. 16 and Supplementary Table 8). The KIE values of approximately 1 for Rh/Al<sub>2</sub>O<sub>3</sub> and Rh/24.5W are consistent with CO insertion into the Rh–C<sub>2</sub>H<sub>5</sub> bond controlling the rate of propanal formation, suggesting that these catalysts exhibit similar reaction mechanisms<sup>23</sup>. The KIE of approximately 2 for Rh/0.7W suggests a rate-controlling step for propanal formation that involves adsorbed H or H<sub>2</sub> (ref. <sup>25</sup>).

The distinct kinetic behaviour of Rh/0.7W, with maintained Rh(CO)<sub>2</sub> presence under the reaction conditions, indicates a unique reaction mechanism on Rh-W pair sites. Ethylene hydroformylation on atomically dispersed Rh, and Rh-W pair sites on SiO<sub>2</sub>, showed a similar influence of W as on Al<sub>2</sub>O<sub>3</sub> (Supplementary Fig. 17 and Supplementary Table 9), suggesting that all kinetically relevant steps occur on Rh-W pair sites.

Rate laws measured at 1 bar predict that higher total pressure and lower temperature would preferentially benefit rate and selectivity for Rh-W pair sites (Supplementary Fig. 18 and Supplementary Table 10). Above approximately 10 bar total pressure, Rh/Al<sub>2</sub>O<sub>3</sub> exhibited increased propanol formation rates and decreased propanal formation rates, indicating metallic Rh cluster formation (Fig. 2c and Supplementary Figs. 13, 19 and 20). Rh-WO<sub>x</sub> pair site formation and Rh localization on 3D WO<sub>x</sub> promoted the stability of atomically dispersed Rh up to 25 bar. Comparisons of propanal selectivity and formation TOF at 1 and 10 bar (at which Rh was atomically dispersed in all catalysts) highlight the particularly beneficial role of increased pressure for Rh/0.7W

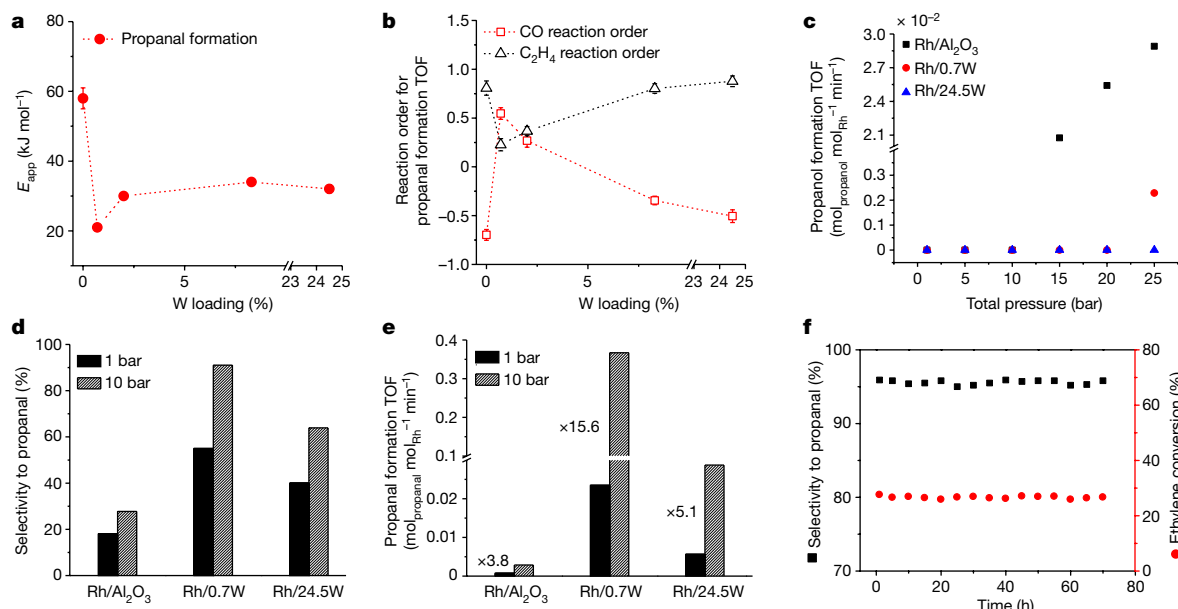


**Fig. 2 | Distinct catalytic behaviour of Rh-WO<sub>x</sub> pair sites.** **a**, Apparent activation energy ( $E_{app}$ ) for propanal formation as a function of W loading in Rh/xW-Al<sub>2</sub>O<sub>3</sub> measured in the temperature range 393–434 K at a total pressure of 1 bar. Error on  $E_{app}$  estimates is the 95% confidence interval of the fit. **b**, CO and C<sub>2</sub>H<sub>4</sub> reaction orders for propanal formation TOF measured at 423 K as a function of W. Error bars refer to standard deviations obtained from three measurements by reloading fresh samples into the reactor. **c**, Propanal formation TOF at 423 K as a function of reactor total pressure. **d**, **e**, Propanal selectivity (**d**) and propanal formation (**e**) TOF at 1 bar and 10 bar at 403 K.

For **a–d**, 60 mg of Rh/xW-Al<sub>2</sub>O<sub>3</sub> catalyst was diluted with 1 g SiO<sub>2</sub> and reduced in CO at 523 K for 1 h and then exposed to a 1:1:1 molar ratio of H<sub>2</sub>, C<sub>2</sub>H<sub>4</sub> and CO with a total flow rate of 30 sccm. **f**, Ethylene conversion and propanal selectivity as a function of time at 373 K and 10 bar for Rh/0.7W. A portion of 420 mg Rh/0.7W-Al<sub>2</sub>O<sub>3</sub> catalyst mixed with 4 g SiO<sub>2</sub> was reduced under CO at 523 K for 1 h and then activated under a 1:1:1 molar ratio of H<sub>2</sub>, C<sub>2</sub>H<sub>4</sub> and CO with a total flow rate of 30 sccm at 423 K and 1 bar. After activation, the catalyst was exposed to a 1:1:1 molar ratio of H<sub>2</sub>, C<sub>2</sub>H<sub>4</sub> and CO with a total flow rate of 15 sccm at 373 K and 10 bar total pressure.

(Fig. 2d,e). Propanal formation TOF increased 16× for Rh/0.7W due to increased pressure, whereas TOFs for Rh/Al<sub>2</sub>O<sub>3</sub> and Rh/24.5W increased approximately 4–5 times.

Using larger catalyst loadings of Rh/0.7W and operating at 373 K and 10 bar, 96% propanal selectivity at an ethylene conversion of 28% and propanal formation rate of approximately 0.1 g<sub>propanal</sub> cm<sup>-3</sup> h<sup>-1</sup> (see

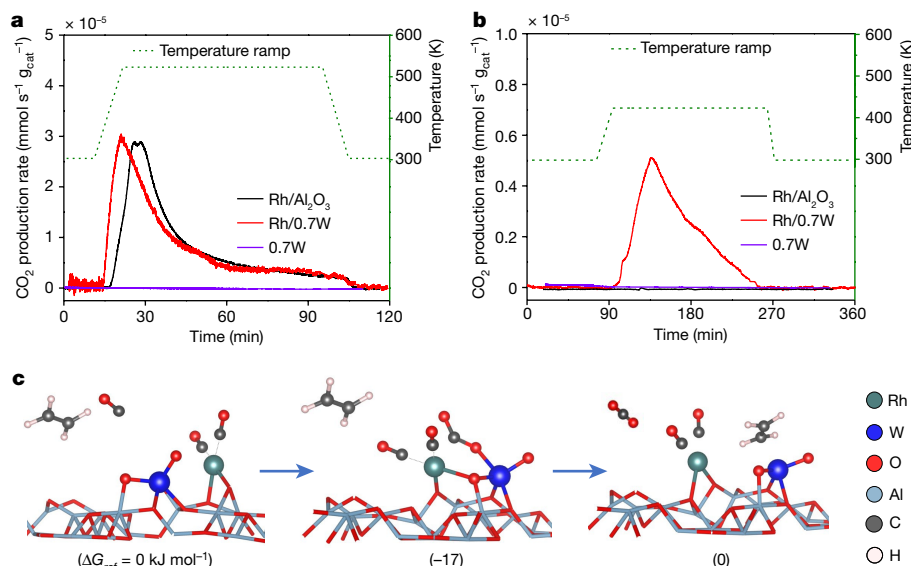


**Fig. 3 | Pair site activation mechanism.** **a**, **b**, CO<sub>2</sub> production rate on Rh/Al<sub>2</sub>O<sub>3</sub>, Rh/0.7W and 0.7W-Al<sub>2</sub>O<sub>3</sub> during CO reduction with 10 sccm CO and 5 sccm He as inert standard (**a**) and during hydroformylation with 10 sccm CO, 10 sccm H<sub>2</sub>, 10 sccm C<sub>2</sub>H<sub>4</sub> and 5 sccm He, following CO reduction (**b**). The inset in each plot shows the temperature program used during analyses. **c**, Mechanism and energetics of the surface mono-oxo W<sup>6+</sup> reduction by CO. The Rh(CO)<sub>2</sub> species

coordinate a third CO molecule, which enables conversion of mono-oxo W<sup>6+</sup> species into a di-oxo geometry that undergoes facile reduction to W<sup>5+</sup> through CO<sub>2</sub> evolution. Also shown is ethylene coordination to W<sup>5+</sup> following CO<sub>2</sub> formation and desorption. (Free energy values of each state are shown in kJ mol<sup>-1</sup> below each image.)

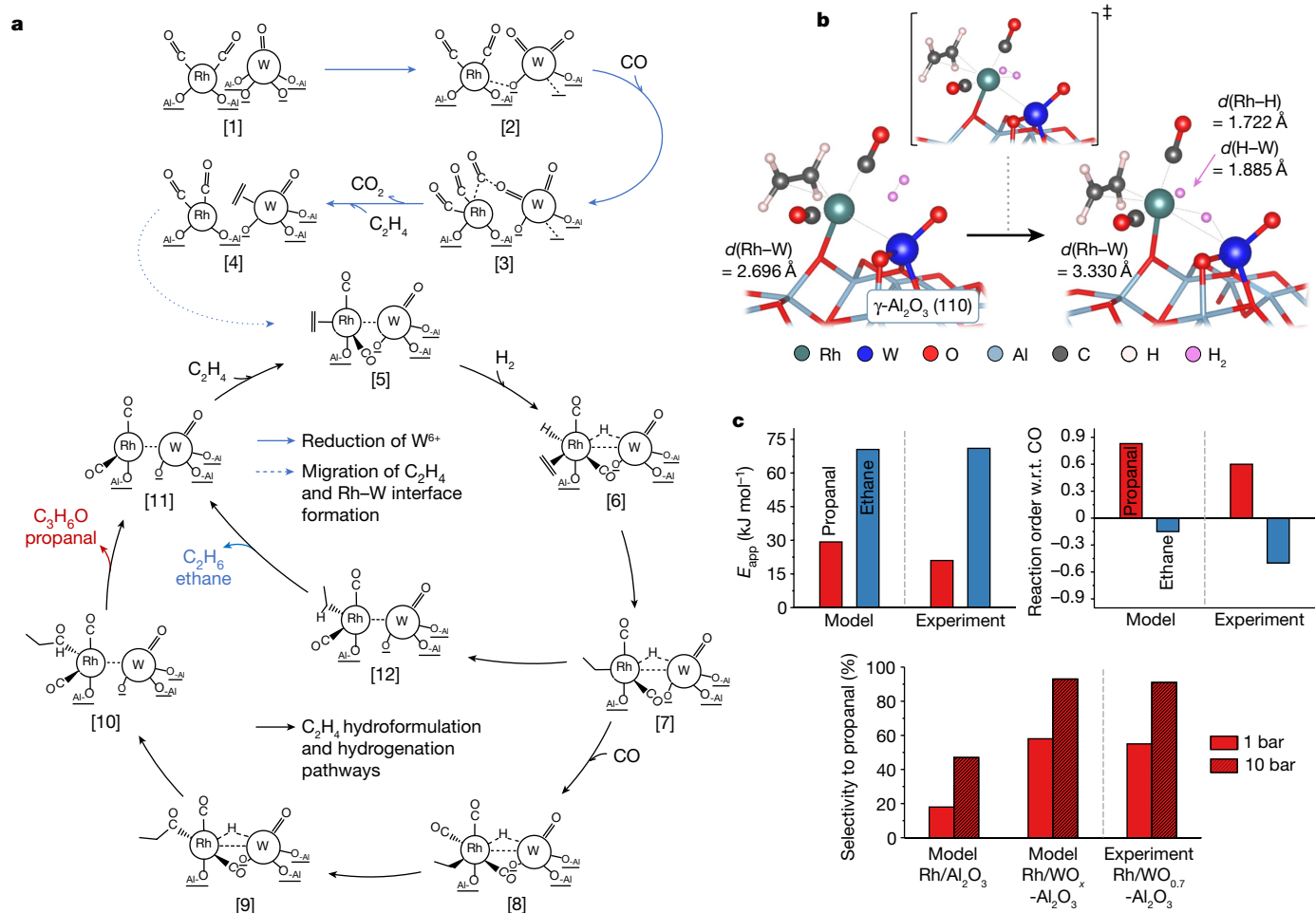


**Fig. 4 | Hydroformylation mechanism and kinetic simulations.**

**a**, Mechanism of  $W^{6+}$  reduction by CO and catalytic cycles for ethylene hydroformylation and hydrogenation on Rh-WO<sub>x</sub> pair site. In contrast to Rh/Al<sub>2</sub>O<sub>3</sub>, activation of the catalyst does not require desorption of a CO ligand, and  $H_2$  activation occurs at the Rh-W interface. **b**, The activated state of the catalyst after ethylene migration from W to Rh, formation of Rh-W bond ( $d(Rh-W) \approx 2.7 \text{ \AA}$ ) and  $H_2$  coordination at the interface of the Rh-W bond (left);

the cooperative binuclear  $H_2$  dissociation transition state (middle); dissociated  $2H^*$  on Rh atom and Rh-W interface (right). **c**, Comparison of kinetic parameters from experiment and microkinetic simulations: apparent activation energy,  $E_{app}$  (top left); reaction order with respect to (w.r.t.) CO for product formation (top right); selectivity to propanal at 1 and 10 bar total pressure on Rh/Al<sub>2</sub>O<sub>3</sub> and Rh-WO<sub>x</sub> pair site at 403 K (bottom).

Supplementary Note 2)<sup>26</sup> were stable for 70 h, which is among the best performances reported in the literature (Fig. 2f, Supplementary Figs. 21–23 and Supplementary Table 1). Measurements of the influence of total pressure on Rh/0.7W reactivity, as well as the independence of propanal selectivity on conversion (Supplementary Figs. 19–21), suggest that higher volumetric propanal formation rates at higher conversion should be feasible, provided that the reaction exothermicity does not drive Rh sintering.

### Active-site formation

During reduction of Rh/Al<sub>2</sub>O<sub>3</sub> and Rh/0.7W with CO at 523 K, transient CO<sub>2</sub> production with a stoichiometry of 2:1 CO<sub>2</sub>:Rh was observed (Fig. 3a and Supplementary Fig. 24). The lack of CO<sub>2</sub> formation for 1W/Al<sub>2</sub>O<sub>3</sub> demonstrates that CO reduced Rh<sup>3+</sup> to Rh<sup>1+</sup> to form Rh(CO)<sub>2</sub> on Rh/Al<sub>2</sub>O<sub>3</sub> and Rh/0.7W, consistent with FTIR and X-ray absorption near edge structure measurements (see Supplementary Fig. 3). Lower temperature CO<sub>2</sub> formation for Rh/0.7W shows that WO<sub>x</sub> promoted the rate of Rh reduction.

During initial exposure of Rh/0.7W to hydroformylation conditions, transient CO<sub>2</sub> evolution was observed at a 1:1 CO<sub>2</sub>:Rh stoichiometry (Fig. 3b), whereas no CO<sub>2</sub> evolved from Rh/Al<sub>2</sub>O<sub>3</sub> or 1W/Al<sub>2</sub>O<sub>3</sub>. The 1:1

CO<sub>2</sub>:Rh stoichiometry demonstrates that a majority of Rh species were paired with W in Rh/0.7W (W:Rh molar ratio was 2:1 and Rh had been reduced to Rh(CO)<sub>2</sub>), and that Rh was required for WO<sub>x</sub> reduction. In situ ultraviolet–visible (UV–vis) measurements indicate that WO<sub>x</sub> species paired with Rh were reduced from +6 to +5 during activation (Supplementary Fig. 25)<sup>20</sup>. CO and C<sub>2</sub>H<sub>4</sub> were both required for WO<sub>x</sub> reduction in Rh-W pair sites (Supplementary Fig. 26).

Density functional theory (DFT) calculations of five distinct atomically dispersed Rh-W pairs were carried out on  $\gamma$ -Al<sub>2</sub>O<sub>3</sub>(110), which is the most exposed facet of  $\gamma$ -Al<sub>2</sub>O<sub>3</sub> (Supplementary Figs. 27–29 and Supplementary Tables 11 and 12)<sup>27</sup>. A model system consisting of Rh<sup>1+</sup>(CO)<sub>2</sub> and W<sup>6+</sup>(=O)(-O)<sub>2</sub>, sitting adjacent to each other on Al<sub>2</sub>O<sub>3</sub> was chosen as representative of the experiments, on the basis of its low energy, the vibrational frequency of Rh(CO)<sub>2</sub>, the feasibility of W<sup>6+</sup> reduction, the reaction mechanism and comparison to X-ray absorption spectroscopy (XAS) measurements (Supplementary Note 3, Supplementary Fig. 30 and Supplementary Tables 13 and 14).

The energetically most favourable hydroformylation pathway on the Rh-W pair site requires reduction of W<sup>6+</sup> to W<sup>5+</sup> (see Supplementary Note 4). During reduction, WO<sub>x</sub> must assume the di-oxo configuration W<sup>6+</sup>(=O)<sub>2</sub>(-O)<sub>2</sub>. This isomerization is more favourable for the Rh-W pair site ( $\Delta_{iso}G = 32 \text{ kJ mol}^{-1}$ ) than WO<sub>x</sub>/Al<sub>2</sub>O<sub>3</sub> ( $\Delta_{iso}G = 140 \text{ kJ mol}^{-1}$ )



because the reducing CO molecule is stabilized by coordinating to one oxo group and Rh(CO)<sub>2</sub> (Fig. 3c). CO<sub>2</sub> evolution requires an activation energy of 220 kJ mol<sup>-1</sup> on WO<sub>x</sub>/Al<sub>2</sub>O<sub>3</sub>, whereas it requires only 62 kJ mol<sup>-1</sup> on the Rh-W pair site. During hydroformylation, WO<sub>x</sub> reduction (WO<sub>x</sub> + CO + C<sub>2</sub>H<sub>4</sub> → WO<sub>(x-1)</sub> + C<sub>2</sub>H<sub>4</sub> + CO<sub>2</sub>) is thermoneutral on Rh-W pair sites ( $\Delta_{\text{red}}G \approx 0$  kJ mol<sup>-1</sup>) because CO<sub>2</sub> evolution is followed by C<sub>2</sub>H<sub>4</sub> binding to W<sup>5+</sup>, which is consistent with experimental observations of CO and C<sub>2</sub>H<sub>4</sub> being required for WO<sub>x</sub> reduction<sup>14</sup>. For WO<sub>x</sub>/Al<sub>2</sub>O<sub>3</sub>, coordination of C<sub>2</sub>H<sub>4</sub> to W<sup>5+</sup> does not make W<sup>6+</sup> reduction feasible ( $\Delta_{\text{red}}G = 89$  kJ mol<sup>-1</sup>) (Supplementary Table 15). These results corroborate the experiments and demonstrate how Rh facilitated WO<sub>x</sub> reduction by CO to form the active Rh-W pair site (see Supplementary Figs. 31–34).

## Bifunctional reaction mechanism

We developed mechanisms for ethylene hydroformylation and hydrogenation on Rh-W pair sites, compared them to Rh/Al<sub>2</sub>O<sub>3</sub> and simulated the microkinetics. Here, we discuss the two kinetically dominant pathways from the five investigated (see Fig. 4a, Supplementary Note 5 and Supplementary Fig. 35).

Initiation of the catalytic cycle on Rh/Al<sub>2</sub>O<sub>3</sub> requires CO desorption from Rh(CO)<sub>2</sub> (the resting state) to enable ethylene adsorption. This is not required on Rh-W pair sites. Instead, ethylene migrates from W to Rh and relaxes *trans* to W (4 → 5 in Fig. 4a) simultaneously with Rh-W bond formation ( $d_{\text{Rh-W}} = 2.7$  Å). The oxidative addition of H<sub>2</sub> occurs through initial coordination to Rh, followed by interfacial H-H activation, which disrupts the Rh-W bond ( $d_{\text{Rh-W}} = 3.3$  Å) and results in one terminal hydride on Rh and one bridging hydride between Rh and W ( $d_{\text{Rh-H}} = 1.7$  and  $d_{\text{W-H}} = 1.9$  Å; Fig. 4b).

At the next stage of the catalytic cycle, hydrometallation engages the terminal hydride on Rh (6 → 7), creating a vacant site that enables coordination of a third CO (7 → 8). The ensuing acylation (8 → 9) and propanal elimination (9 → 10), which involves the bridging hydride, complete the hydroformylation catalytic cycle. The hydrogenation pathway branches off at complex 7 (see Supplementary Fig. 36 and Supplementary Table 14 for the reaction free energies).

Microkinetic simulation (Supplementary Note 6 and Supplementary Tables 17 and 18) of Rh-W pair sites at 423 K predict  $E_{\text{app}}$  values of 29 and 71 kJ mol<sup>-1</sup> for hydroformylation and hydrogenation, respectively (Fig. 4c and Supplementary Table 19). Kinetic justification for the low  $E_{\text{app}}$  value is provided in Supplementary Note 6. The hydroformylation rate is controlled by acylation (control coefficient,  $X_{\text{RC}} = 0.7$ ) and H<sub>2</sub> oxidative addition ( $X_{\text{RC}} = 0.6$ ) (Supplementary Table 20). DFT predicts that H<sub>2</sub> addition gives rise to a primary KIE of 1.96, whereas CO insertion gives rise to a secondary KIE of 1.40, due to the bridging hydride, resulting in an overall KIE of 1.8. A KIE of 1.03 is predicted for propanal formation on Rh/Al<sub>2</sub>O<sub>3</sub>, as the rate is controlled by acylation ( $X_{\text{RC}} = 0.9$ ). DFT predictions of KIEs for hydrogenation are provided in Supplementary Note 7 and Supplementary Tables 8 and 21. The simulated propanal formation rate on Rh-W pair sites exhibits  $\alpha_{\text{CO,propanal}} = 0.8$ , in contrast with Rh/Al<sub>2</sub>O<sub>3</sub> (refs.<sup>21,23,28</sup>) (Fig. 4c and Supplementary Notes 5–7). Predictions of propanal selectivity on Rh-W pair sites showed an increase from 45% at 1 bar and 423 K, to 93% at 10 bar and 403 K (Fig. 4c and Supplementary Table 19).

Accurate predictions of experimental active-site formation and kinetic observables by DFT-based microkinetic simulations provide confidence in the mechanistic insights (Supplementary Note 8). Rh-W pair sites facilitate high selectivity hydroformylation and alleviate CO poisoning of Rh (positive  $\alpha_{\text{CO,propanal}}$ ) to enable high rates by dynamically reconfiguring their coordination during the catalytic cycle. Rh-W pair sites: (1) enable W<sup>6+</sup> reduction and formation of the active Rh-W site; (2) transfer adsorbed ethylene from W to Rh without the typically required CO desorption step; and (3) dissociate H<sub>2</sub> at the Rh-W interface to produce a bridging hydride between Rh and W that facilitates

adsorption of a third CO on Rh before acylation, which facilitates CO insertion and propanal formation. The dynamic reconfiguration of the Rh-W pair during the catalytic cycle is thus critical for high rates and selectivity, which is consistent with the behaviour of Rh supported in phosphine layers (Supplementary Table 1)<sup>29</sup>. Furthermore, similarities between the proposed elementary steps here and those on binuclear homogeneous catalysts<sup>10</sup> and metal–support interfaces<sup>30</sup> highlight how atomically dispersed pair sites enable analysis of bifunctional reaction pathways.

The bifunctional Rh-WO<sub>x</sub> pair site is surprising given the lack of similar behaviour for Rh-ReO<sub>x</sub> pair sites<sup>21,23</sup>. Unfavourable thermodynamics for ReO<sub>x</sub> reduction in Rh-ReO<sub>x</sub> pairs (Supplementary Fig. 34 and Supplementary Note 4) show that pair site structures and the energetics of pair site reconfiguration can dictate when emergent bifunctional mechanisms occur. Consistent with this, not all theoretically explored Rh-WO<sub>x</sub> pair sites exhibited feasible WO<sub>x</sub> reduction (Supplementary Table 15 and Supplementary Note 4). These comparisons suggest that the geometry of the Rh-WO<sub>x</sub> interface, inter-site communication and the energetics of adaptive restructuring during the reaction mechanism are critical for bifunctional behaviour. Recent analysis showed that achieving catalytic benefits from bifunctional active sites beyond those achievable by a single optimal active site, requires cooperation between active-site types that follow different linear free energy relationships<sup>31–34</sup>. Our observations suggest that descriptors attempting to predict the existence of bifunctional reaction mechanisms must consider both structural and chemical information for the reactive interfaces.

## Online content

Any methods, additional references, Nature Research reporting summaries, source data, extended data, supplementary information, acknowledgements, peer review information; details of author contributions and competing interests; and statements of data and code availability are available at <https://doi.org/10.1038/s41586-022-05075-4>.

1. Cao, L. et al. Atomically dispersed iron hydroxide anchored on Pt for preferential oxidation of CO in H<sub>2</sub>. *Nature* **565**, 631–635 (2019).
2. Saavedra, J. et al. The critical role of water at the gold-titania interface in catalytic CO oxidation. *Science* **345**, 1599–1602 (2014).
3. Lam, E. et al. CO<sub>2</sub> hydrogenation on Cu/Al<sub>2</sub>O<sub>3</sub>: role of the metal/support interface in driving activity and selectivity of a bifunctional catalyst. *Angew. Chem. Int. Ed.* **58**, 13989–13996 (2019).
4. Shekhar, M. et al. Size and support effects for the water–gas shift catalysis over gold nanoparticles supported on model Al<sub>2</sub>O<sub>3</sub> and TiO<sub>2</sub>. *J. Am. Chem. Soc.* **134**, 4700–4708 (2012).
5. Carrasquillo-Flores, R. et al. Reverse water–gas shift on interfacial sites formed by deposition of oxidized molybdenum moieties onto gold nanoparticles. *J. Am. Chem. Soc.* **137**, 10317–10325 (2015).
6. Kattel, S., Liu, P. & Chen, J. G. Tuning selectivity of CO<sub>2</sub> hydrogenation reactions at the metal/oxide interface. *J. Am. Chem. Soc.* **139**, 9739–9754 (2017).
7. Zhao, Z. J. et al. Importance of metal–oxide interfaces in heterogeneous catalysis: a combined DFT, microkinetic, and experimental study of water–gas shift on Au/MgO. *J. Catal.* **345**, 157–169 (2017).
8. Blasco, T. et al. Carbonylation of methanol on metal-acid zeolites: evidence for a mechanism involving a multisite active center. *Angew. Chem. Int. Ed.* **46**, 3938–3941 (2007).
9. Campos, J. Bimetallic cooperation across the periodic table. *Nat. Rev. Chem.* **4**, 696–702 (2020).
10. Hetterscheid, D. G. H. et al. Binuclear cooperative catalysts for the hydrogenation and hydroformylation of olefins. *ChemCatChem* **5**, 2785–2793 (2013).
11. Garland, M. The catalytic binuclear elimination reaction: importance of non-linear kinetic effects and increased synthetic efficiency. *Top. Organomet. Chem.* **59**, 187–231 (2015).
12. Alexeev, O., Shelef, M. & Gates, B. C. MgO-supported platinum–tungsten catalysts prepared from organometallic precursors: platinum clusters isolated on dispersed tungsten. *J. Catal.* **164**, 1–15 (1996).
13. Matsubu, J. C. et al. Adsorbate-mediated strong metal–support interactions in oxide-supported Rh catalysts. *Nat. Chem.* **9**, 120–127 (2017).
14. Lwin, S. et al. Nature of WO<sub>x</sub> sites on SiO<sub>2</sub> and their molecular structure–reactivity/selectivity relationships for propylene metathesis. *ACS Catal.* **6**, 3061–3071 (2016).
15. Matsubu, J. C., Yang, V. N. & Christopher, P. Isolated metal active site concentration and stability control catalytic CO<sub>2</sub> reduction selectivity. *J. Am. Chem. Soc.* **137**, 3076–3084 (2015).

16. Sparta, M., Børve, K. J. & Jensen, V. R. Activity of rhodium-catalyzed hydroformylation: added insight and predictions from theory. *J. Am. Chem. Soc.* **129**, 8487–8499 (2007).
  17. Li, C., Wang, W., Yan, L. & Ding, Y. A mini review on strategies for heterogenization of rhodium-based hydroformylation catalysts. *Front. Chem. Sci. Eng.* **12**, 113–123 (2018).
  18. Mol, J. C. Industrial applications of olefin metathesis. *J. Mol. Catal. A* **213**, 39–45 (2004).
  19. Ross-Medgaarden, E. I. & Wachs, I. E. Structural determination of bulk and surface tungsten oxides with UV–vis diffuse reflectance spectroscopy and raman spectroscopy. *J. Phys. Chem. C* **111**, 15089–15099 (2007).
  20. Barton, D. G. et al. Structure and electronic properties of solid acids based on tungsten oxide nanostructures. *J. Phys. Chem. B* **103**, 630–640 (1999).
  21. Ro, I. et al. Synthesis of heteroatom Rh–ReO<sub>x</sub> atomically dispersed species on Al<sub>2</sub>O<sub>3</sub> and their tunable catalytic reactivity in ethylene hydroformylation. *ACS Catal.* **9**, 10899–10912 (2019).
  22. Rice, C. A. et al. The oxidation state of dispersed Rh on Al<sub>2</sub>O<sub>3</sub>. *J. Chem. Phys.* **74**, 6487–6497 (1981).
  23. Lee, S. et al. Theoretical study of ethylene hydroformylation on atomically dispersed Rh/Al<sub>2</sub>O<sub>3</sub> catalysts: reaction mechanism and influence of ReO<sub>x</sub> promoter. *ACS Catal.* **11**, 9506–9518 (2021).
  24. Perez-Aguilar, J. E. et al. Isostructural atomically dispersed rhodium catalysts supported on SAPO-37 and on HY zeolite. *J. Am. Chem. Soc.* **142**, 11474–11485 (2020).
  25. Brundage, M. A. & Chuang, S. S. C. Experimental and modeling study of hydrogenation using deuterium step transient response during ethylene hydroformylation. *J. Catal.* **164**, 94–108 (1996).
  26. Lange, J. P. Performance metrics for sustainable catalysis in industry. *Nat. Catal.* **4**, 186–192 (2021).
  27. Digne, M. et al. Hydroxyl groups on  $\gamma$ -alumina surfaces: a DFT study. *J. Catal.* **211**, 1–5 (2002).
  28. Navidi, N., Thybaut, J. W. & Marin, G. B. Experimental investigation of ethylene hydroformylation to propanal on Rh and Co based catalysts. *Appl. Catal. A* **469**, 357–366 (2014).
  29. Shylesh, S. et al. In situ formation of Wilkinson-type hydroformylation catalysts: insights into the structure, stability, and kinetics of triphenylphosphine- and xantphos-modified Rh/SiO<sub>2</sub>. *ACS Catal.* **3**, 348–357 (2013).
  30. Whittaker, T. et al. H<sub>2</sub> oxidation over supported Au nanoparticle catalysts: evidence for heterolytic H<sub>2</sub> activation at the metal–support interface. *J. Am. Chem. Soc.* **140**, 16469–16487 (2018).
  31. Baz, A. & Holewinski, A. Understanding the interplay of bifunctional and electronic effects: microkinetic modeling of the CO electro-oxidation reaction. *J. Catal.* **384**, 1–13 (2020).
  32. Darby, M. T. et al. Lonely atoms with special gifts: breaking linear scaling relationships in heterogeneous catalysis with single-atom alloys. *J. Phys. Chem. Lett.* **9**, 5636–5646 (2018).
  33. Andersen, M. et al. Analyzing the case for bifunctional catalysis. *Angew. Chem. Int. Ed.* **55**, 5210–5214 (2016).
  34. Kumar, G. et al. Multicomponent catalysts: limitations and prospects. *ACS Catal.* **8**, 3202–3208 (2018).
- Publisher's note** Springer Nature remains neutral with regard to jurisdictional claims in published maps and institutional affiliations.
- Springer Nature or its licensor holds exclusive rights to this article under a publishing agreement with the author(s) or other rightsholder(s); author self-archiving of the accepted manuscript version of this article is solely governed by the terms of such publishing agreement and applicable law.
- © The Author(s), under exclusive licence to Springer Nature Limited 2022

## Methods

### Catalyst preparation

$\gamma$ -Al<sub>2</sub>O<sub>3</sub> nanoparticles (US Research Nanomaterials, catalogue no. US3007) and mesoporous SBA-15 (SiO<sub>2</sub>) with 4 nm pore size (Sigma-Aldrich, catalogue no. 7631-86-9) were used as the supports. W was deposited on Al<sub>2</sub>O<sub>3</sub> via incipient wetness impregnation with ammonium metatungstate hydrate, ((NH<sub>4</sub>)<sub>6</sub>H<sub>2</sub>W<sub>12</sub>O<sub>40</sub>·xH<sub>2</sub>O, Sigma-Aldrich, 99.99%) in an aqueous solution. The impregnated samples were dried at room temperature overnight, then calcined at 773 K for 4 h, as described in detail elsewhere<sup>14</sup>. W-Al<sub>2</sub>O<sub>3</sub> samples prepared are denoted as xW-Al<sub>2</sub>O<sub>3</sub>, where *x* is equal to the actual W loading and the W surface density was calculated using equation (1).

$$\text{W surface density [atoms/nm}^2\text{]} = \frac{\text{Actual W weight loading} \times \text{Avogadro's number} \left[ \frac{\text{atoms}}{\text{mol}} \right]}{\text{Surface area of support} \left[ \frac{\text{m}^2}{\text{g}} \right] \times \text{W molar weight} \left[ \frac{\text{g}}{\text{mol}} \right]} \quad (1)$$

For the deposition of Rh species, appropriate amounts of Rh precursor, tris(ethylenediamine) rhodium(III) chloride (Alfa Aesar, catalogue no. 10553) were dissolved in 6 ml of high-performance liquid chromatography (HPLC)-grade water (J.T. Baker, catalogue no. JT4218-3) and the pH of the precursor solution was adjusted through dropwise addition of NH<sub>4</sub>OH or HNO<sub>3</sub> (ref. <sup>21</sup>). In a typical synthesis, 0.1 g of support was suspended in 24 ml of HPLC-grade water under magnetic stirring and the pH of the suspension was adjusted with NH<sub>4</sub>OH or HNO<sub>3</sub>. The pH values of the precursor and support solutions were equivalent in all syntheses and are shown in Supplementary Table 2. The 6 ml Rh precursor solution (concentration of 10 or 50 ppm) was mixed with the 24 ml support suspension under magnetic stirring, and stirred for 1 h, with a surface loading of 470 m<sup>2</sup> L<sup>-1</sup> (see equation (2)). After stirring, the mixture was filtered using 0.45 μm membrane filters and the solid was dried overnight at 303 K and calcined at 623 K before carrying out reactivity measurements or characterization. Prepared catalysts were stored in a desiccator in a closed vial. Hereafter, Rh/W-Al<sub>2</sub>O<sub>3</sub> samples were referred to as Rh/xW-Al<sub>2</sub>O<sub>3</sub>, where *x* is the actual W loading measured by inductively coupled plasma atomic emission spectroscopy (ICP-AES).

$$\text{Surface loading} \left[ \frac{\text{m}^2}{\text{L}} \right] = \frac{\text{Surface area of support} \left[ \frac{\text{m}^2}{\text{g}} \right] \times \text{support mass [g]}}{\text{Total volume of solution [L]}} \quad (2)$$

For the deposition of atomically dispersed Rh species onto SiO<sub>2</sub>, appropriate amounts of the rhodium precursor were dissolved in 10 ml of HPLC-grade water and desired amounts of triethanolamine (TEA, Sigma-Aldrich, catalogue no. 90278) (TEA/Rh molar ratio of 8:1) were added into the solution under magnetic stirring for 30 min (ref. <sup>35</sup>). The Rh precursor solution was injected via a syringe pump (5 ml h<sup>-1</sup>) into a 100 ml suspension of the SiO<sub>2</sub> support under magnetic stirring. After mixing for 12 h at room temperature, the solution was dried at 353 K using a rotary evaporator. For the synthesis of atomically dispersed Rh-W pair sites on SiO<sub>2</sub>, appropriate amounts of ((NH<sub>4</sub>)<sub>6</sub>H<sub>2</sub>W<sub>12</sub>O<sub>40</sub>·xH<sub>2</sub>O) were dissolved in 10 ml of HPLC-grade water and the desired amounts of TEA (TEA/W molar ratio of 8:1) were added into the solution under magnetic stirring for 30 min. Appropriate amounts of the Rh precursor were then added into the solution, and the mixture was stirred for another 30 min. The precursor solution was injected via a syringe pump (5 ml h<sup>-1</sup>) into a 100 ml suspension of the SiO<sub>2</sub> support under magnetic stirring. After being mixed for 12 h at room temperature, the solution was dried at 353 K using a rotary evaporator. The prepared catalysts

were calcined at 723 K for 4 h under dry air before characterization and reactivity measurements.

Control samples containing exclusively Rh nanoparticles on Al<sub>2</sub>O<sub>3</sub> with 10% Rh weight loading were synthesized following methods reported previously<sup>36</sup>.

### Catalyst characterization

**FTIR spectroscopy.** Catalysts were loaded into a Harrick Praying Mantis low-temperature reaction chamber with ZnSe windows mounted inside a Thermo Scientific Praying Mantis diffuse reflectance adapter set inside a Thermo Scientific Nicolet iS10 FTIR spectrometer with a mercury cadmium telluride detector cooled by liquid nitrogen. Spectra were obtained by averaging 64 spectra at a resolution of 4 cm<sup>-1</sup>. Spectra are presented in absorbance using the following relationship: absorbance = log  $\frac{1}{R'}$ , where *R'* is relative reflectance, which is the measured quantity<sup>37</sup>. All gases were passed across an isopropyl alcohol/liquid nitrogen cold trap and a glass trap filled with Drierite desiccant to remove trace moisture.

For CO FTIR characterization, catalysts were oxidized in situ at 623 K for 1 h under an O<sub>2</sub> flow, followed by in situ reduction under 10% H<sub>2</sub> flow balanced with He at 473 K for 1 h. After pretreatment, catalysts were cooled to subambient temperature (148 K) under Ar, and then a baseline spectrum was taken before introduction of CO. An atmosphere of 10% CO/90% Ar was introduced to the catalyst until the spectra stabilized (approximately 10 min) for saturation CO adsorption, and then purged with 100 sccm Ar for 10 min. The interaction strength between CO and Rh was probed in TPD experiments. In the TPD experiments the temperature was ramped from room temperature to 673 K at a rate of 20 K min<sup>-1</sup> in 100 sccm of Ar flow.

For pyridine FTIR, catalysts were oxidized in situ at 623 K for 1 h under an O<sub>2</sub> flow, followed by in situ pretreatment under 10% CO flow balanced with He at 523 K for 1 h. A baseline spectrum was collected after pretreatment and then pyridine was introduced to the catalyst by flowing Ar through a pyridine bubbler and purged with 100 sccm Ar for 10 min to remove physisorbed pyridine.

For in situ FTIR measurements, catalysts were oxidized in situ at 623 K for 1 h under an O<sub>2</sub> flow, followed by in situ reduction under 10% CO flow balanced with He at 473 K for 1 h. The spectra of catalysts were collected at 423 K under a reactant mixture of equimolar C<sub>2</sub>H<sub>4</sub>, H<sub>2</sub> and CO with 30 sccm total flow rate after 5 min, 1 h and 15 h at 443 K. Shown for comparison are spectra collected at 293 K under Ar after 15 h under the reactions conditions.

**Brunauer–Emmett–Teller.** The support surface area was estimated from nitrogen adsorption data at 77 K using a Micromeritics 3Flex Porosimeter. Samples were degassed at 523 K overnight before Brunauer–Emmett–Teller measurements.

**UV–vis diffuse reflectance spectroscopy.** UV–vis diffuse reflectance spectra of W-Al<sub>2</sub>O<sub>3</sub> were obtained using dehydrated MgO as a reference with a Thermo Scientific Evolution 300 UV–vis spectrometer equipped with a Harrick Scientific Praying Mantis diffuse reflectance accessory. Samples were lightly ground using a pestle and mortar and dehydrated at 723 K for 1 h in flowing dry air, as described in detail elsewhere<sup>20,38</sup>. The Kubelka–Munk function (*F(R<sub>∞</sub>)*) was calculated using equations (3) and (4), as reported previously<sup>20,38</sup>.

$$\text{Reflectance}(R)_{\infty} = \frac{R_{\text{sample}}}{R_{\text{MgO}}} \quad (3)$$

$$F(R)_{\infty} = \frac{(1 - R_{\infty})^2}{2R_{\infty}} \quad (4)$$

The onset of photon absorption induced by the ligand to metal charge transfer in each sample was determined by finding the *x* axis intercept

# Article

of the straight line in the graph with  $h\nu$  as the  $x$  axis and  $[F(R_{\infty})h\nu]^2$  as the  $y$  axis. The ligand to metal charge transfer onset for reference compounds representing isolated and oligomeric  $\text{WO}_x$  was obtained from previous studies and included for comparison.

**ICP-AES spectroscopy.** The Rh uptake efficiency and Rh loading on supports were determined using a Thermo iCAP 6300 ICP emission spectrometer. The filtrate obtained after catalyst synthesis was analysed with ICP-AES to determine Rh uptake, calculated from the difference in the Rh concentration in solution before and after interaction with the support (see equation (5)).

$$\begin{aligned} \text{Rh uptake efficiency (\%)} \\ = \frac{(\text{Rh concentration}_{\text{initial}} - \text{Rh concentration}_{\text{final}})}{(\text{Rh concentration}_{\text{initial}})} \times 100 \quad (5) \end{aligned}$$

For the determination of Rh loading, 30–70 mg of catalyst was digested with aqua regia (a mixture of 3 ml of nitric acid and 9 ml of hydrochloric acid) under magnetic stirring by refluxing at 353 K for 14 h. W loading was measured by the amount of W leached into the aqueous solution during Rh deposition synthesis. The post-digestion mixture was cooled down to room temperature and filtered using 0.45  $\mu\text{m}$  syringe filter PTFE membranes (Corning, catalogue no. 431231) and then used for ICP analysis.

**Point of zero charge measurements.** The surface charge behaviours of  $\text{Al}_2\text{O}_3$  and  $\text{W-Al}_2\text{O}_3$  were determined by measuring the point of zero charge (PZC). For the measurement of PZC, six bottles of 0.01 M NaCl solution were prepared with HPLC-grade water. The initial pH values of these solutions were adjusted to 2, 4, 6, 8, 10 and 12 using 0.1 M HCl and 0.1 M NaOH solution after 2 h He bubbling to remove dissolved gases. Then, 75 mg of the samples were suspended in 25 ml of HPLC-grade water under magnetic stirring in airtight conditions, and the final pH of the suspension was measured after 24 h stirring. The initial pH versus final pH was plotted, and the value obtained at the intersection of the data with the  $y = x$  line gives the PZC.

**Raman spectroscopy.** Raman spectroscopy experiments were carried out using a Horiba XploRA Plus confocal Raman microscope with an air-cooled solid-state 473 nm (excitation) laser. Before obtaining Raman measurements, calibration was carried out using a silicon wafer. All measurements used a 2,400 grating  $\text{mm}^{-1}$  grating (spectral resolution  $\leq 3 \text{ cm}^{-1}$ ) with a laser power of 100% at 473 nm and a  $10\times$  objective (working distance: 10.6 mm). In situ Raman studies used a high-temperature cell (HVC-MRA-5) and a dome equipped with a quartz window from Harrick Scientific. Approximately 10–20 mg of sample was used for each in situ experiment. The sample was calcined in situ at 623 K ( $50 \text{ cm}^3$  (STP)  $\text{min}^{-1}$ ) and was kept at 300 K under Ar flow for spectral acquisition.

**HAADF-STEM microscopy.** High-angle annular dark-field scanning transmission electron microscopy (HAADF-STEM) was performed on a JEOL Grand ARM300CF microscope at 300 kV. The images were collected using a convergence semi-angle of 34 mrad, and inner and outer collection angles of 79 and 180 mrad, respectively. A beam current of 23 pA was used with a pixel time of 4  $\mu\text{s}$ . The images for all samples were collected after ex situ CO pretreatment at 523 K. Energy-dispersive X-ray spectroscopy (EDS) mapping results were acquired using the dual large angle EDS detectors equipped in the same microscope.

**Temperature-programmed reduction.** Temperature-programmed reduction (TPR) was carried out using a Micromeritics AutoChem II 2920. Before TPR, samples were pretreated under  $\text{O}_2$  flow at 773 K for 1 h. A TPR run was carried out in a flow of 10%  $\text{H}_2/\text{Ar}$  mixture gas at a flow rate of  $50 \text{ ml min}^{-1}$  with a temperature ramp of  $10 \text{ K min}^{-1}$ . An isopropyl alcohol/liquid nitrogen cold trap was installed to remove

moisture from the TPR effluent stream before the stream entered a thermal conductivity detector. The consumption of hydrogen was monitored as a function of temperature using the thermal conductivity detector.

**In situ XAS spectroscopy.** The in situ XAS experiments were carried out at beamline 7-BM (QAS) of the National Synchrotron Light Source II (NSLS-II) at Brookhaven National Laboratory. The Rh K edge (23,220 eV) and W L3 edge (10,207 eV) XAS spectra were collected for the RhW/ $\text{Al}_2\text{O}_3$  catalyst, as well as for metal foils (Rh and W) and metal oxide standards ( $\text{Rh(III)}_2\text{O}_3$ ,  $\text{Rh(I)}(\text{CO})_2(\text{acac})$ ,  $\text{W(V)}_2\text{O}_5$  and  $\text{W(VI)}\text{O}_3$ ). The in situ experiments were performed using a Clausen cell as described in a previous report<sup>39</sup>. Approximately 50 mg of sample (80–100 mesh) was loaded into a polyimide tube (internal diameter: 2.0 mm, outer diameter: 2.4 mm) that enabled simultaneous collection of the transmission and fluorescence signals. The catalyst bed was fixed by two pieces of quartz wool on both sides. The sample was reduced with 5 vol% CO ( $40 \text{ ml min}^{-1}$ ) in He at 523 K for 2 h and then cooled to 423 K in the same atmosphere. The hydroformylation reaction was carried out at 423 K by exposing the sample to a mixture of  $\text{C}_2\text{H}_4$  ( $2 \text{ ml min}^{-1}$ ), CO (5 vol%,  $40 \text{ ml min}^{-1}$ ) and  $\text{H}_2$  ( $2 \text{ ml min}^{-1}$ ) for 4.5 h. For each process, the XAS data were continuously collected and the multiple scans with the identical feature were merged as an individual spectrum to improve the signal-to-noise ratio. Data processing was performed using the IFEFFIT package<sup>40</sup>. Rh and W foils were used as standard references for energy calibration and to obtain the passive electron reduction factor ( $S_0^2$ ). Fittings of the W L3 edge extended X-ray absorption fine structure spectra were performed on the basis of the phase shifts and back-scattering amplitudes obtained from the DFT-optimized models.

## Reactivity and kinetic measurements

The catalytic activity for ethylene hydroformylation was evaluated in a fixed-bed reactor with an inner and outer diameters of 7 and 12 mm, respectively, in the temperature range 403–443 K at atmospheric pressure, as described in detail previously<sup>21</sup>. An ultra-high purity-grade reactant gas mixture of  $\text{C}_2\text{H}_4$ ,  $\text{H}_2$  and CO at a molar ratio of 1:1:1 was used with a total flow rate of  $30 \text{ cm}^3$  (STP)  $\text{min}^{-1}$ . The CO gas was housed in an aluminium-lined cylinder to avoid potential contamination by iron and nickel carbonyls. The CO gas was also passed through a purifier made with silica chips (silicon dioxide, fused, 4–20 mesh, Sigma-Aldrich) in a 3/8 inch outer diameter stainless steel tube at 623 K to remove any metal carbonyls from the CO feed<sup>41</sup>. Before reactivity measurements, catalysts were pretreated in situ under a CO flow of  $10 \text{ cm}^3$  (STP)  $\text{min}^{-1}$  at 523 K for 1 h. Typically, 60 mg catalysts were diluted with 1 g of  $\text{SiO}_2$  (acid purified silicon dioxide, Sigma-Aldrich, catalogue no. 84878) for kinetic measurement and 420 mg catalyst was diluted with 4 g  $\text{SiO}_2$  to achieve the high conversion. The TOF was calculated using the number of Rh sites assuming that all Rh was atomically dispersed.

The activation mechanism of catalysts was studied by monitoring the  $\text{CO}_2$  production rate under CO reduction and hydroformylation conditions. The catalysts were in situ oxidized at 623 K under  $\text{O}_2$ , then exposed to the CO reduction conditions (5 sccm He and 10 sccm CO) at 523 K and then the hydroformylation conditions (5 sccm He, 10 sccm CO, 10 sccm  $\text{H}_2$  and 10 sccm  $\text{C}_2\text{H}_4$ ) at 423 K. All gases were passed across an isopropyl alcohol/liquid nitrogen cold trap and a glass trap filled with Drierite desiccant to remove trace moisture. The produced  $\text{CO}_2$  ( $m/z = 44$ ) was quantified with online mass spectrometry (HALO 201, Hiden Analytical). To understand which reactants activated Rh/0.7W, a similar process was applied. Rh/0.7W was oxidized for 1 h at 623 K under  $\text{O}_2$  and then reduced under CO for 1 h at 523 K. After the reduction, the catalyst was exposed to a mixture of 5 sccm Ar, 10 sccm CO and 10 sccm  $\text{H}_2$ , a mixture of 5 sccm Ar, 10 sccm CO and 10 sccm  $\text{C}_2\text{H}_4$ , and a mixture of 5 sccm Ar, 10 sccm CO, 10 sccm  $\text{H}_2$  and 10 sccm  $\text{C}_2\text{H}_4$ , sequentially at 423 K.  $\text{CO}_2$  formation was quantified by online mass spectrometry.



## Isotopic labelling experiments

Catalysts were oxidized at 623 K for 1 h and then reduced at 523 K for 1 h under CO. After activation at 423 K with the reactant gas mixture of C<sub>2</sub>H<sub>4</sub>, H<sub>2</sub> and CO at a molar ratio of 1:1:1 with a total flow rate of 30 cm<sup>3</sup> (STP) min<sup>-1</sup>, catalysts were exposed to C<sub>2</sub>H<sub>4</sub>, H<sub>2</sub> and CO for 2 h at 403 K, and then the stream was switched to equimolar C<sub>2</sub>H<sub>4</sub>, D<sub>2</sub> (deuterium, Sigma, catalogue no. 361860) and CO with a total flow rate of 30 sccm for 1 h. The stream was switched back to unlabelled H<sub>2</sub>. The ethane and propanal formation rates were measured by online gas chromatography. The KIE was calculated by comparing the production rates with H<sub>2</sub> and D<sub>2</sub> reactants.

## DFT calculations

Periodic-DFT calculations were used to model the Rh-W pair sites on  $\gamma$ -Al<sub>2</sub>O<sub>3</sub>(110), which is the most exposed facet of  $\gamma$ -Al<sub>2</sub>O<sub>3</sub> (refs. <sup>42,43</sup>). The  $\gamma$ -Al<sub>2</sub>O<sub>3</sub>(110) surface was represented by a four-layer (bottom layer fixed) 1 × 2 slab separated by its periodic image in the z direction by a vacuum region of 15 Å; the physical dimensions of the 1 × 2 slab were 8.33 × 16.02 × 20 Å<sup>3</sup>. Spin-polarized periodic-DFT calculations were performed at the Perdew–Burke–Erzenhof<sup>44</sup> theory level with D3 dispersion (zero damping) of Grimme et al.<sup>45</sup> and dipole corrections. The projector-augmented wave<sup>46,47</sup> method was used to model core electrons. Conventional valence configurations were used for all elements except Rh and W, for which the semicore *p* states and *s* states were also included in the valence shell, respectively ('Rh\_pv' and 'W\_sv' in Vienna ab-initio simulation package (VASP)). For all structures, an energy cut-off of 400 eV (600 eV for bulk) was used. The Brillouin zone was sampled on 4 × 2 × 1 *k*-point grids for this study. Gaussian smearing of 0.1 eV width was used. The SCF iterations were converged to 10<sup>-6</sup> eV and geometries were optimized to 0.01 eV Å<sup>-1</sup> and 0.05 eV Å<sup>-1</sup> for bulk and slab calculations, respectively. Transition states were located by the climbing-image NEB method<sup>46,47</sup>, converged to 0.05 eV Å<sup>-1</sup>, and confirmed by vibrational frequency analysis. All DFT calculations were performed with VASP (v.5.4.1)<sup>44</sup>.

## Microkinetic modelling

Microkinetic modelling was performed using CHEMKIN<sup>48</sup>. Thermal corrections to the electronic energies were obtained within the harmonic oscillator approximation using the Python multiscale thermochemistry toolbox (pMuTT)<sup>49</sup>. Reaction conditions were chosen to match those in the experiments<sup>21</sup>: 393–443 K, atmospheric pressure, reactant gas mixture of C<sub>2</sub>H<sub>4</sub>, H<sub>2</sub> and CO at a molar ratio of 1:1:1 and total flow rate of 30 cm<sup>3</sup> (STP) min<sup>-1</sup>. All microkinetic model parameters and results are provided in Supplementary Note 5.

## Data availability

Source data associated with all theoretical and experimental analysis are provided with this paper. The data and code necessary to build the DFT-based microkinetic model that supports the plots in this paper are available on Zenodo at <https://doi.org/10.5281/zenodo.6525676>. Any other data in the supplementary information will be provided by the corresponding author upon request.

35. Qi, J. et al. Selective methanol carbonylation to acetic acid on heterogeneous atomically dispersed ReO<sub>4</sub>/SiO<sub>2</sub> catalysts. *J. Am. Chem. Soc.* **142**, 14178–14189 (2020).
36. Hoffman, A. J. et al. Theoretical and experimental characterization of adsorbed CO and NO on  $\gamma$ -Al<sub>2</sub>O<sub>3</sub>-supported Rh nanoparticles. *J. Phys. Chem. C* **125**, 19733–19755 (2021).
37. Sirta, J., Phanichphant, S. & Meunier, F. C. Quantitative analysis of adsorbate concentrations by diffuse reflectance FT-IR. *Anal. Chem.* **79**, 3912–3918 (2007).
38. Lwin, S. et al. Surface ReO<sub>x</sub> sites on Al<sub>2</sub>O<sub>3</sub> and their molecular structure–reactivity relationships for olefin metathesis. *ACS Catal.* **5**, 1432–1444 (2015).
39. Chupas, P. J. et al. A versatile sample–environment cell for non-ambient X-ray scattering experiments. *J. Appl. Crystallogr.* **41**, 822–824 (2008).
40. Ravel, B. & Newville, M. ATHENA, ARTEMIS, HEPHAESTUS: data analysis for X-ray absorption spectroscopy using IFEFFIT. *J. Synchrotron Radiat.* **12**, 537–541 (2005).
41. Ro, I. et al. The role of Pt–Fe<sub>2</sub>O<sub>3</sub> interfacial sites for CO oxidation. *J. Catal.* **358**, 19–26 (2018).
42. Perdew, J. P., Burke, K. & Ernzerhof, M. Generalized gradient approximation made simple. *Phys. Rev. Lett.* **77**, 3865–3868 (1996).
43. Grimme, S., Antony, J., Ehrlich, S. & Krieg, H. A consistent and accurate ab initio parametrization of density functional dispersion correction (DFT-D) for the 94 elements H–Pu. *J. Chem. Phys.* **132**, 154104 (2010).
44. Kresse, G. & Furthmüller, J. Efficiency of ab-initio total energy calculations for metals and semiconductors using a plane-wave basis set. *Comput. Mater. Sci.* **6**, 15–50 (1996).
45. Blöchl, P. E. Projector augmented-wave method. *Phys. Rev. B* **50**, 17953–17979 (1994).
46. Sheppard, D., Terrell, R. & Henkelman, G. Optimization methods for finding minimum energy paths. *J. Chem. Phys.* **128**, 134106 (2008).
47. Sheppard, D. et al. A generalized solid-state nudged elastic band method. *J. Chem. Phys.* **136**, 074103 (2012).
48. Coltrin, M. E., Kee, R. J., Rupley, F. M. & Meeks, E. *SURFACE CHEMKIN-III: A Fortran Package for Analyzing Heterogeneous Chemical Kinetics at a Solid-surface–Gas-phase Interface* Report SAND96-8217 (Sandia, 1996).
49. Lym, J., Wittreich, G. R. & Vlachos, D. G. A Python multiscale thermochemistry toolbox (pMuTT) for thermochemical and kinetic parameter estimation. *Comput. Phys. Commun.* **247**, 106864 (2020).

**Acknowledgements** I.R., J.Q., S.L., D.G.V., S.C. and P.C. acknowledge the Catalysis Center for Energy Innovation, an Energy Frontier Research Center funded by the US Department of Energy, Office of Science, Office of Basic Energy Sciences under award number DE-SC0001004. M.X., X.Y. and X.P. acknowledges the NSF awards under grant nos CBET-2031494 and CHE-1955786 for support for the microscopy. This research used 7-BM (QAS) beamline of the National Synchrotron Light Source II, a US DOE Office of Science User Facility operated for the DOE Office of Science by Brookhaven National Laboratory under contract no. DE-SC0012704. Beamline operations were supported in part by the Synchrotron Catalysis Consortium (US DOE, Office of Basic Energy Sciences, grant no. DE-SC0012335). I.R. acknowledges the National Research Foundation of Korea (NRF) grant funded by The Ministry of Science and ICT (MSIT) (NRF-2021R1F1A1054980). The authors acknowledge the use of facilities and instrumentation at the UC Irvine Materials Research Institute (IMRI) supported in part by the NSF through the MRSEC program (DMR-2011967). We acknowledge A. B. Getsioan for providing the 10% Rh/Al<sub>2</sub>O<sub>3</sub> Rh nanoparticle control sample. J. Resasco is acknowledged for his comments on the paper.

**Author contributions** I.R. and J.Q. synthesized, characterized and evaluated the reactivity of all catalysts. S.L. executed all theoretical analyses. M.X. and X.Y. performed all microscopy. Z.X. performed XAS measurements and associated data analysis. G.Z. designed and built the high-pressure reactor. A.M. helped develop catalyst synthesis methodologies. J.G.C. oversaw the XAS measurements and analysis. X.P. oversaw the microscopy and analysis. D.G.V. and S.C. oversaw the theoretical calculations and analysis. P.C. conceived and managed the overall project. All authors contributed to writing the manuscript.

**Competing interests** The authors declare no competing interests.

### Additional information

**Supplementary information** The online version contains supplementary material available at <https://doi.org/10.1038/s41586-022-05075-4>.

**Correspondence and requests for materials** should be addressed to Phillip Christopher.

**Peer review information** Nature thanks Tiefeng Wang and Mie Andersen for their contribution to the peer review of this work.

**Reprints and permissions information** is available at <http://www.nature.com/reprints>.